Computational Materials Science 246 (2025) 113384

Contents lists available at ScienceDirect

Computational Materials Science

journal homepage: www.elsevier.com/locate/commatsci

Full length article

Interstitals as non-radiative recombination centers for all-inorganic halide perovskites

Yijun Tong [a,*], Xiaofeng Xiang [b], Scott Dunham [a]

[a] Department of Electrical and Computer Engineering, University of Washington, Seattle, 98195, WA, USA
[b] Molecular Engineering & Sciences Institute, University of Washington, Seattle, 98195, WA, USA

ARTICLE INFO

Keywords:
Perovskites
DFT
Non-radiative recombination

ABSTRACT

Inorganic halide perovskites have been considered as higher-stability alternatives to hybrid halide perovskites for optoelectronic applications. However, the formation of defects in these materials can significantly affect carrier density and recombination lifetime. Thus, understanding their properties is of great importance for achieving improved device performance. Through GGA+U calculations with spin–orbital coupling, we calculate the properties of native defects in $CsPbI_3$/$CsSnI_3$ and the defect-assisted non-radiative recombination rates for selected deep levels. Importantly, we discover that the iodine interstitials in $CsPbI_3$ and tin interstitials in $CsSnI_3$ have high non-radiative carrier capture rates. Besides, we also notice that complete defect structural relaxations are only achievable when large supercells are used. This work not only provides insights into potential non-radiative recombination pathways due to the formation of corresponding interstitials, but also highlights the importance of utilizing large supercells for defect calculations in perovskites.

1. Introduction

Hybrid organic–inorganic halide perovskites (ABX_3), represented by methylammonium lead/tin iodide $MAPbI_3$/$MASnI_3$ (CH_3NH_3) with FA ($CH[NH_2]_2$) and/or Cs alloyed on the A-sites, have attracted enormous attention in the past years for photovoltaic (PV) applications [1], because of their high power-conversion efficiencies [2] (over 25%) and low-cost fabrication methods [3]. Perovskites are also promising materials for light emitting diodes [4] (LEDs) and photodetectors [5]. However, the potential applications of hybrid organic–inorganic halide perovskites are restricted by degradation due to ambient environment such as humidity and oxygen [6]. Due to the reasons stated above, all-inorganic halide perovskites, such as $CsPbI_3$ and $CsSnI_3$, which possess not only outstanding optoelectronic properties but also enhanced stability, have been considered as alternatives to their hybrid counterparts [7].

Understanding native defects and impurities is critical for these applications in order to control doping levels and carrier lifetime. Theoretical calculations based on density functional theory (DFT) have been performed to study the nature of native defects in halide perovskites, yet no common computational setup have been agreed upon to deliver reliable calculation results and conclusions [8,9]. Previous literature reports that the spin–orbital coupling (SOC) effect is essential to reliably predicting not only the band gap values, but also the correct competition between electronic and elastic relaxation energies of defects in perovskites [10]. However, defect calculations are limited to utilizing relatively small supercells when applying hybrid functional including SOC. Furthermore, the finite-size corrections for charged defects are sometimes neglected without clear reasons [10,11].

The underestimation of band gap values (with SOC) for perovskites employing (semi)local exchange–correlation functionals is a well-known issue. So far, only hybrid density functionals with adjusted mixing parameter of the exchange interaction are able to accurately predict the band gap values [12–14]. However, not only applying hybrid functionals with SOC is very computationally expensive, which limits the size of supercell for defect calculations, but also the adjustment of mixing parameter is semi-empirical. Yang et al. applied ACBN0 and eACBN0 methods in QUANTUM ESPRESSO [15] to self-consistently calculated the onsite U and intersite V Hubbard parameters of three types of halide perovskites based on PBE optimized structures, and improved band gap accuracy were obtained by applying these Hubbard parameters [16]. However, simultaneous convergence of both Hubbard parameters and lattice parameters were only achieved for bond disproportionated halide perovskites. Paul et al. studied the undoped and doped cubic phase $CsSnCl_3$ using GGA+U in the Cambridge Serial Total Energy Package (CASTEP) [17] with empirical effective Hubbard U values added on the s and p orbitals of Cs, Sn and Cl as well as d orbitals of doping elements [18]. In practice, the applied U values depend

---

* Corresponding author.
E-mail address: yijunt@uw.edu (Y. Tong).

https://doi.org/10.1016/j.commatsci.2024.113384
Received 18 July 2024; Received in revised form 13 September 2024; Accepted 15 September 2024

strongly on the software, pseudopotentials, computational setups, and thus need to be carefully tested.

In this work, we present a first-principles study on native defects of γ-CsPbI$_3$ and γ-CsSnI$_3$ using GGA+U including SOC. Band gap values and structural parameters that are comparable to results from hybrid functionals calculations are obtained, based on which large supercells for defect calculations are created for defect calculations. Defect thermodynamic transition levels (TLs) and defect formation energies (DFEs) under different conditions of chemical potentials are calculated. Among selected native point defects, we determine those that have the potential to behave as deep traps based on calculated TLs and perform carrier capture calculations for iodine interstitials in γ-CsPbI$_3$ and tin interstitials in γ-CsSnI$_3$ based on anharmonic one-dimensional configuration coordinate diagrams (CCD). Specifically, our results show that iodine interstitials in γ-CsPbI$_3$ have high non-radiative carrier capture rates, same as reported in previous literature [19]. Tin interstitials in γ-CsSnI$_3$, on the other hand, turn out to be strong minority traps in substrates prepared under Sn-poor condition.

2. Computational methods

Density functional theory calculations are performed in the Vienna ab initio simulation package (VASP) [20], in which the ion-cores are described by the projected augmented wave (PAW) method [21]. The revised Perdew–Burke–Ernzerhof for solids (PBEsol) exchange–correlation functional [22] was employed with the spin–orbital coupling (SOC) effect included in both the electronic calculation and structural relaxation of bulk cells and supercells with defects. The kinetic energy cutoff for plane-wave basis is set to 500 eV. Van der waals energy-correction is included using the DFT-D3 method [23]. Effective Hubbard parameters in the simplified (rotationally invariant) approach [24] are employed on p orbitals of Pb (U_{eff} = 5 eV) in γ-CsPbI$_3$ and Sn (U_{eff} = 4.3 eV) in γ-CsSnI$_3$. For bulk calculations of $\gamma-$CsPbI$_3$ and $\gamma-$CsSnI$_3$ (space group Pnma), a 4 × 4 × 3 gamma-centered k-point mesh is used. 360-atom supercells for defect calculations are constructed for $\gamma-$CsPbI$_3$ and $\gamma-$CsSnI$_3$ respectively by using a 3 × 3 × 2 conversion. A single Γ-point is used in defect calculations, and the atomic structures are relaxed until the residual forces drop below 5 meV/Å. The mixing parameters hybrid functional (HSE) calculations are chosen to be $\alpha = 0.43$ for $\gamma-$CsPbI$_3$ and $\alpha = 0.59$ for $\gamma-$CsPbI$_3$ respectively, as suggested by previous literature [12–14]. SOC is not included in the structural relaxation using HSE due to the limitation of our computational resources.

Defect formation energies (DFE) and defect transition levels are calculated according to the following equations [25]

$$DFE[X^q] = E[X^q] - E_{bulk} - \Sigma_i n_i \mu_i + q(\epsilon_{VB} + \epsilon_F) + E^q_{corr} \tag{1}$$

$$\epsilon(q/q') = \frac{E[X^q] - E[X^{q'}]}{q' - q} + \frac{E^q_{corr} - E^{q'}_{corr}}{q' - q} - \epsilon_{VB} \tag{2}$$

where $E[X^q]$ is the energy of the supercell with defect X in charged state q, E_{bulk} is the energy of the pristine supercell, n and μ are respectively the number and chemical potential of atoms added to or subtracted from the bulk supercell, ϵ_{VB} is the energy of the valence band maximum (VBM), and ϵ_F is the position of the Fermi level with respect to VBM. E^q_{corr} is the charged-cell correction to DFE due to the interaction of localized defect charge in a finite-size supercell with its periodic images, which is calculated in the Freysoldt, Neugebauer and Van de Walle (FNV) correction scheme [26]. Chemical potentials of species and the resulting two-component phase diagrams are calculated following the approach outlined in previous literature [27], and the results are shown in the Appendix.

Table 1
Structural parameters and band gaps from GGA+U and HSE.

	$\gamma-$CsPbI$_3$		$\gamma-$CsSnI$_3$	
	GGA+U	HSE (α = 0.43)	GGA+U	HSE (α = 0.59)
a [Å]	9.18	9.02	9.04	8.77
b [Å]	8.44	8.59	8.35	8.61
c [Å]	12.53	12.48	12.44	12.38
V [Å^3]	970.81	966.97	939.02	934.81
Band gap [eV]	1.63	1.67	1.25	1.29

3. Results and discussion

3.1. Structural parameters and band gap values

In Table 1, we present the results of calculations of the structural parameters and band gap values for both $\gamma-$CsPbI$_3$ and $\gamma-$CsSnI$_3$, using both GGA+U and HSE. Clearly, the lattice constants in c direction as well as the cell volumes are close using both calculation schemes. The lattice parameters calculated using GGA+U are larger in a direction and smaller in b direction compared to HSE, which are probably the consequences of the "structural dilation" issue observed in DFT+U [16]. The band gap values calculated using GGA+U and HSE are fairly close.

The calculated density of states are shown in Figs. 1 and 2. Clearly for both materials the valence band maximums (VBM) are composed of I-p and Pb-s/Sn-s orbitals, and the conduction band maximums (CBM) are mainly for Pb-p/Sn-p orbitals, in agreement with previous literature [14]. The band gap values are corrected due the fact that the Hubbard U values applied on Pb-p/Sn-p orbitals push up the conduction bands.

3.2. Defect calculations of CsPbI$_3$ and CsSnI$_3$

Calculated defect formation energies of selected native point defects in CsPbI$_3$ and CsSnI$_3$ and are shown in Figs. 3 and 4. The concentration of a defect is exponentially dependent on the negative of its corresponding DFE. The calculated defect transition levels are shown in Fig. 5.

For CsPbI$_3$, it is evident that the DFEs of donors are low, thus dominating the defect concentration in Pb-rich condition, resulting an n-type substrate, which agrees with previous literature [28]. Lowering the chemical potential of Pb pushes CsPbI$_3$ toward the intrinsic regime. Noticeably, both the (+1/0) (0.7641 eV below CBM) and (0/-1) (0.3812 eV above VBM) transition levels of I_i are deep, indicating that iodine interstitials can behave as both deep donors and deep acceptors. It is found that both I_i^0 and I_i^{+1} form iodine trimer-like structures by breaking the two Pb-I bonds and moving toward the center of two neighboring iodine atoms. Bonding of the iodine trimer lowers the formation energy of these two charged states and result in deep transition levels. In contrast, I_i^0 and I_i^{+1} in CsSnI$_3$ do not have such trimer-like structures, and thus the transition levels are shallow. Meanwhile, the concentration of iodine interstitials in CsPbI$_3$ are significant under both Pb-moderate and Pb-poor conditions, indicating the potential for behaving as dominating deep traps. The (+2/+1) transition level of Pb_I antisites (0.8 eV below CBM) is deep, and the concentration is significant under Pb-rich condition. Although the formation of iodine interstitials can be suppressed under Pb-rich conditions, the formation of Pb_I will be enhanced correspondingly. Under Pb-rich conditions, the CsPbI$_3$ absorber is n-type and thus the hole capture capability of deep traps dominate the Shockley–Read–Hall non-radiative recombination. Since the concentration of iodine interstitials is not negligible even under Pb-rich conditions, the hole capture rates of both I_i^0 and I_i^{-1} are especially worthy of investigation (see Figs. 6 and 7).

For CsSnI$_3$, the substrate is p-type in Sn-poor conditions due to the high concentration of acceptors, especially tin vacancies, which is in line with previous literature [29,30]. In Sn-rich and Sn-moderate

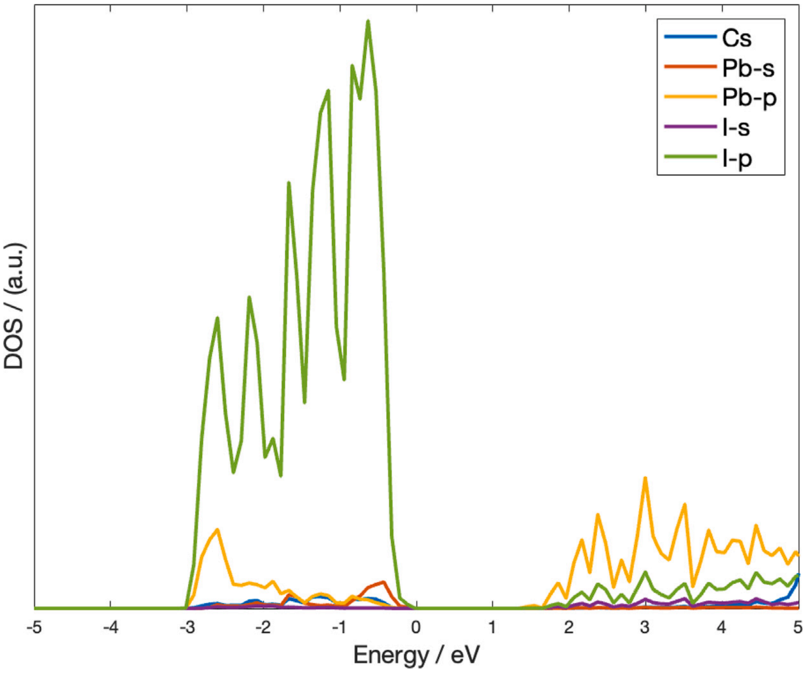

Fig. 1. Calculated DOS of $\gamma-\mathrm{CsPbI_3}$.

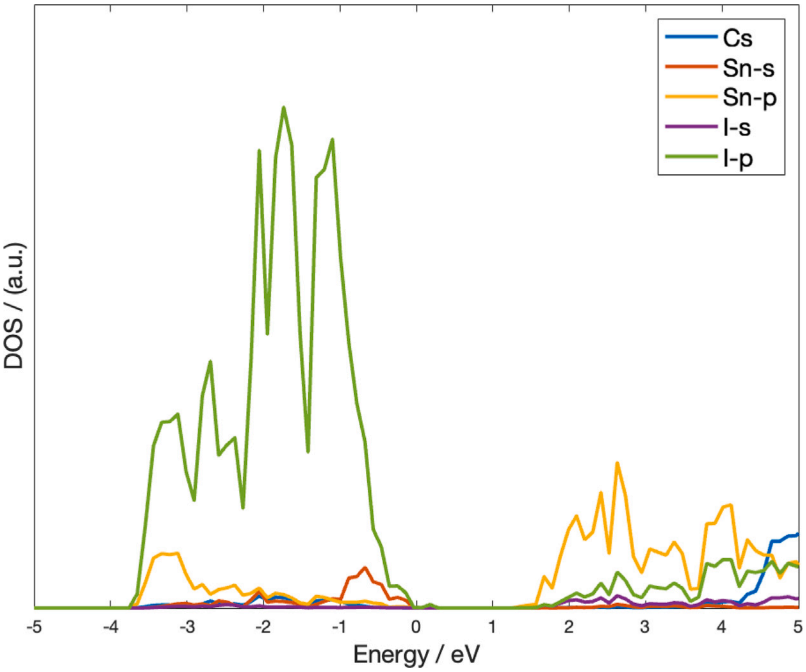

Fig. 2. Calculated DOS of $\gamma-\mathrm{CsSnI_3}$.

conditions, $\mathrm{CsSnI_3}$ is relatively intrinsic, where the concentrations of tin interstitials with deep (+1/0) (0.441 eV below CBM) and (+2/+1) (0.133 eV below CBM) levels increase compared to Sn-poor condition. Looking into the defect structure of tin interstitials, it is found that the number of Sn-I bonds of the interstitial Sn atom is increasing from Sn_i^0 to Sn_i^{+1} and then Sn_i^{+2}, indicating the preference for the formation of Sn-I bonds. In contrast, Pb_i in $\mathrm{CsPbI_3}$ only introduce shallow levels. Investigating the defect structure of the nominal charged state I_i^{-1} of iodine interstitials in both perovskites, the Sn-I bond (3.145 Å) is found to be shorter than the Pb-I bond (3.288 Å). As the net charge of B-site atoms as well as C-site atoms are nearly the same in both perovskites, this result suggests that Sn-I bonding is stronger than Pb-I bonding due to enhanced electrostatic interactions. This deduction is also supported by the above-mentioned absence of the iodine trimer-like structure of I_i^0 and I_i^{+1} in $\mathrm{CsSnI_3}$. On the other hand, acceptors with deep levels of significant concentrations are not found, and thus we believe that the role of acceptors in $\mathrm{CsSnI_3}$ is mainly for self-p-doping (see Fig. 8).

3.3. Defect-assisted carrier capture calculations

The rate of Shockley–Read–Hall recombination induced by defects can be calculated from first-principles [31,32]. In order to further study whether deep levels indeed significantly trap carriers, we calculate the defect-assisted carrier capture coefficients of iodine interstitials in

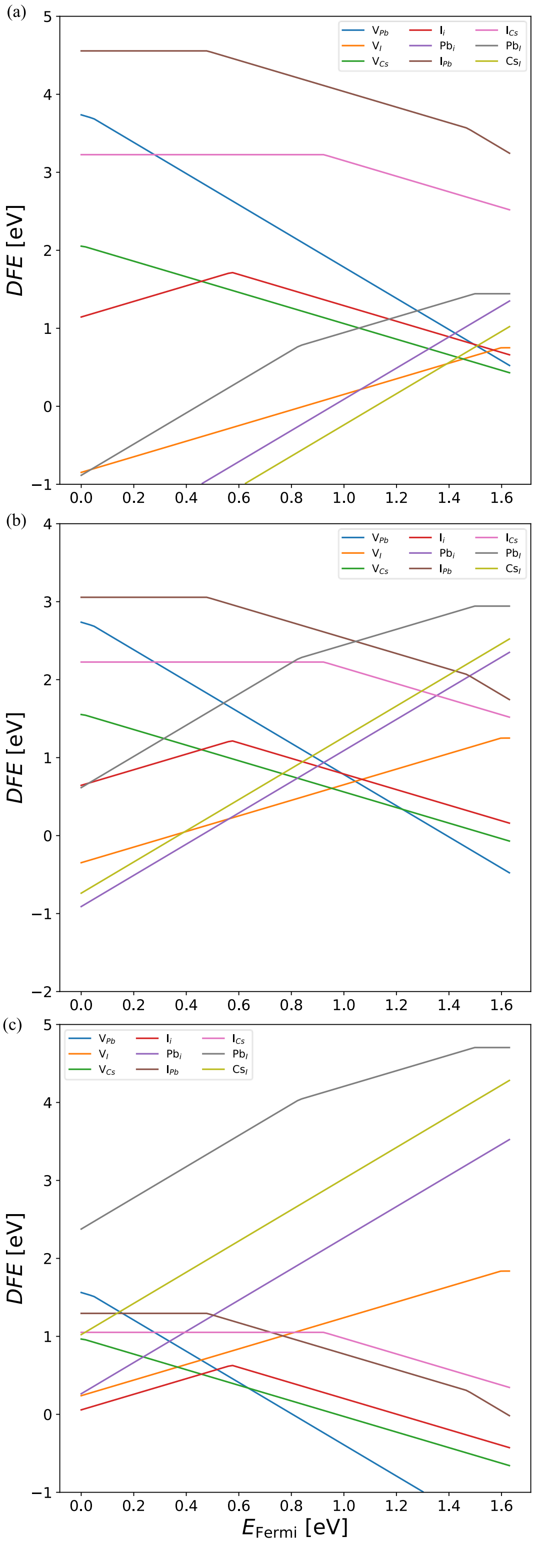

Fig. 3. Calculated defect formation energies (DFE) versus Fermi level of native defects in $CsPbI_3$ under (a) Pb-rich (b) Pb-moderate and (c) Pb-poor condition, respectively.

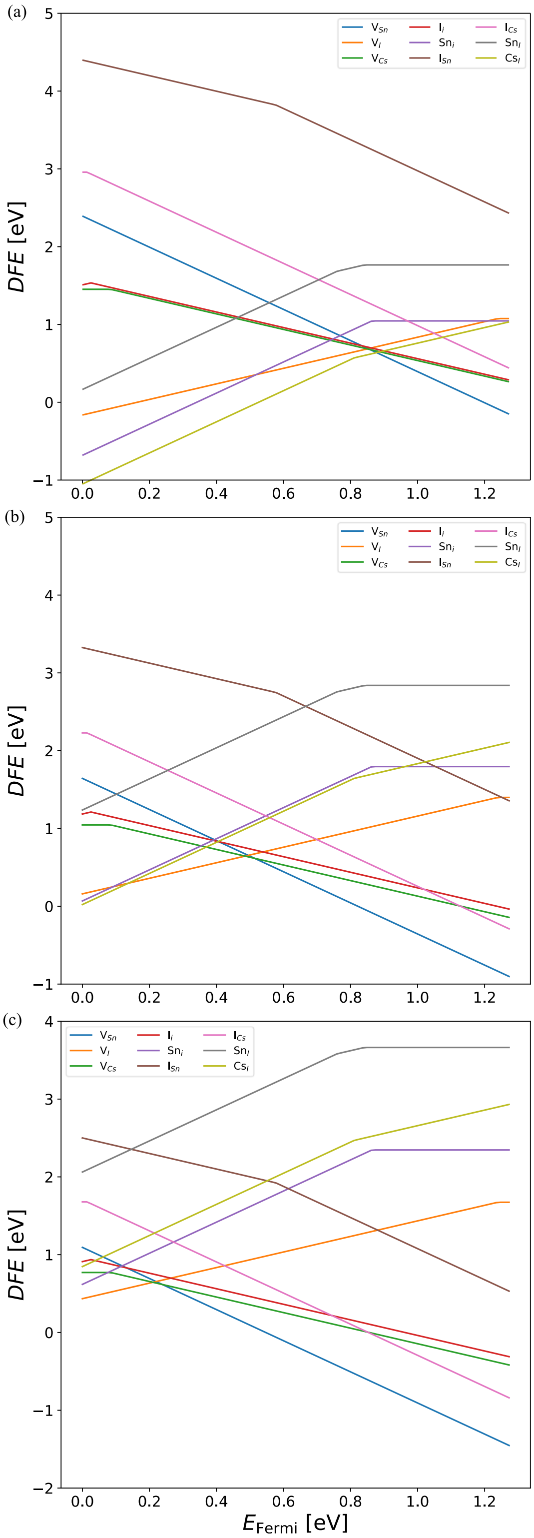

Fig. 4. Calculated defect formation energies (DFE) versus Fermi level of native defects in $CsSnI_3$ under (a) Sn-rich (b) Sn-moderate and (c) Sn-poor condition, respectively.

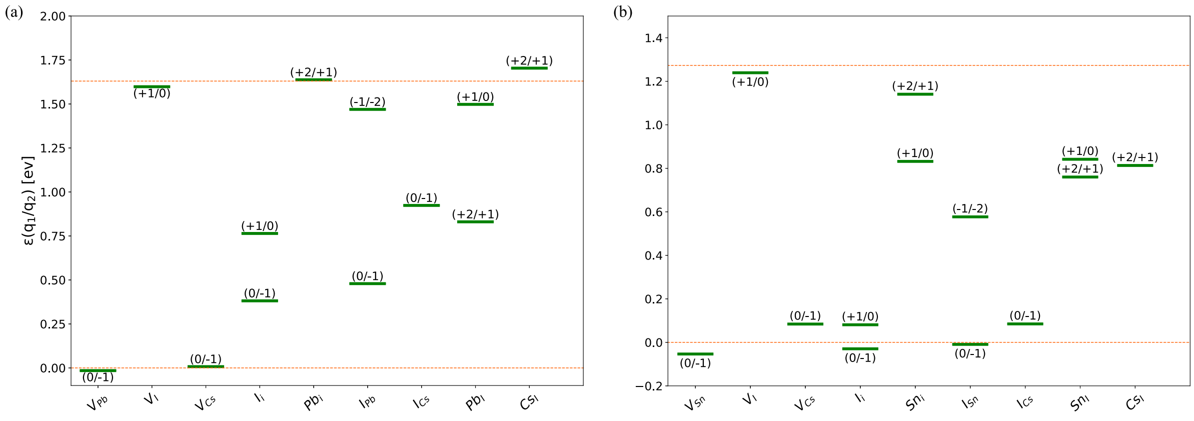

Fig. 5. Defect transition levels of selected native defects in (a) $CsPbI_3$ and (b) $CsSnI_3$.

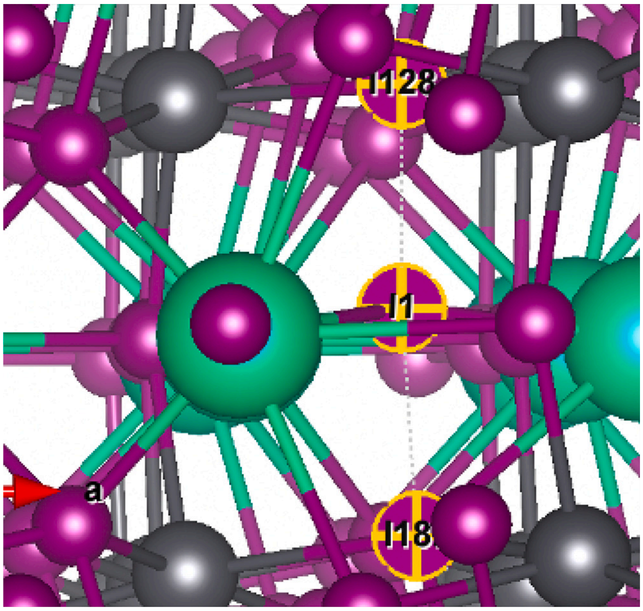

Fig. 6. Local structure of Ii^{+1} in $CsPbI_3$.

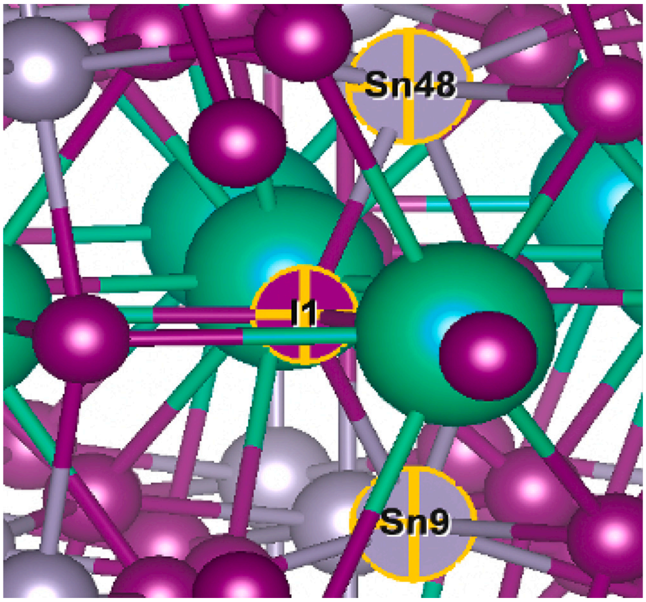

Fig. 7. Local structure of Ii^{+1} in $CsSnI_3$.

Table 2
Carrier capture rate of iodine interstitials in $CsPbI_3$ at 300K.

Transition level	ΔQ[amu$^{1/2}$ Å]	C_n[cm^3 s^{-1}]	C_p[cm^3 s^{-1}]
(0/−1)	30.90	$2.41 * 10^{-9}$	$3.34 * 10^{-7}$
(+1/0)	44.89	$1.33 * 10^{-8}$	$1.22 * 10^{-8}$

Table 3
Carrier capture rate of tin interstitials in $CsSnI_3$ at 300K.

Transition level	ΔQ[amu$^{1/2}$ Å]	C_n[cm^3 s^{-1}]	C_p[cm^3 s^{-1}]
(+1/0)	13.56	$7.10 * 10^{-6}$	$7.24 * 10^{-11}$
(+2/+1)	21.92	$2.83 * 10^{-5}$	$6.31 * 10^{-14}$

$CsPbI_3$ and tin interstitials in $CsSnI_3$ based on the reconstruction of one-dimensional configuration coordinate diagrams (CCD), as shown in Figs. 9 and 10. The distortion between the ground-state structures of two charged-states associated with a single transition level is quantified by the configuration coordinate difference (ΔQ):

$$\Delta Q^2 = \sum_{\alpha} m_\alpha (R_\alpha^f - R_\alpha^i)^2 \tag{3}$$

where m_α, R_α^f and R_α^i are the mass, final and initial Cartesian coordinates of atom α in the defective supercell, respectively. The defect-assisted non-radiative electron and hole capture rate (C_p and C_n) describe the process of a defect capturing an electron from the conduction band edge or a hole from the valence band edge respectively, and can be computed based on Fermi's golden rule:

$$C = \frac{2\pi}{\hbar} g V W_{if}^2 \sum_m w_m \sum_n |\langle \chi_{im}|\hat{Q} - Q_0|\chi_{fn}\rangle|^2 \tag{4}$$

$$\times\ \delta(\Delta E + m\hbar\Omega_i - n\hbar\Omega_f) \tag{5}$$

where χ_{im} and χ_{fn} are the wavefunctions of the mth and nth phononic wave functions in the initial i and final f states. V is the supercell volume, g is the configurational degeneracy and W_{if} is the electron–phonon overlap. w_m is the probability of thermal occupation of the mth phonon state, and Ω_i/Ω_f are the initial/final phonon frequencies. The anharmonic potential energy surfaces (PES) in CCDs are used for obtaining the phonon frequencies as well as the phonon wave functions. A sufficient number of phonon eigenvalues are included (N = 500) in order to guarantee convergence. Finite-size corrections to CCDs are implemented using the methodology proposed by Kumagai [33] (see Fig. 11).

From calculated results shown in Tables 2 and 3, both I_i in $CsPbI_3$ and Sn_i in $CsSnI_3$ show strong carrier capture capabilities. Specifically, both (0/-1) and (+1/0) of I_i show strongly anharmonic PES and large ΔQ values. The similarity of PES around the ground-state structure of excited states (blue curves) indicates strong overlap between phononic

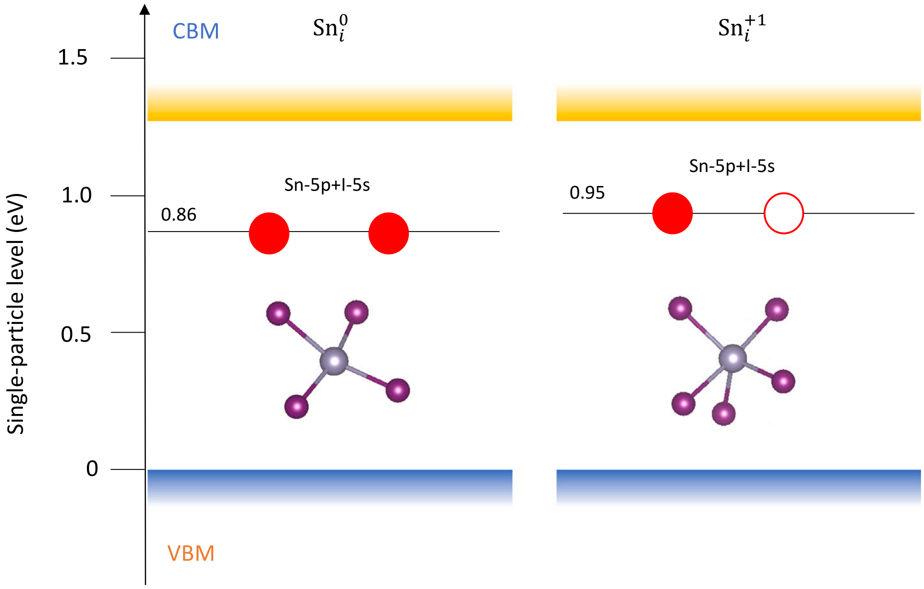

Fig. 8. Single particle levels for Sn_i^0 and Sn_i^{+1}. Local defect structures are shown below the single particle levels.

Table 4
$\Delta Q[\mathrm{amu}^{1/2}$ Å] of (0/−1) and (+1/0) transitions for I_i in CsPbI_3.

	80-atom cell	160-atom cell	360-atom cell	540-atom cell
(0/−1)	35.69	29.72	30.9	30.95
(+1/0)	14.16	45.15	44.89	44.93

wave functions, and thus leads to large hole capture rates, which are especially harmful if n-type CsPbI_3 substrate is present. We notice that our calculated ΔQ values are much larger than what are reported in previous literature [19], and believe that the difference mainly stems from the difference in size of supercells used for defect calculations. In order to verify this, we calculate ΔQ for the (+1/0) transition of I_i using supercells with 80 (2 × 2 × 1), 160 (2 × 2 × 2), 360 (3 × 3 × 2) and 540 (3 × 3 × 3) atoms. As shown in Table 4, ΔQ values are convergent within 0.05 $\mathrm{amu}^{1/2}$Å when the cell size is larger 360 atoms. In the 80-atom cell, the ΔQ values are very different from the converged values, which are likely to be the results of incomplete structure relaxation due to the size limitation. In contrast, the larger supercells allow atoms located far from the defects to relax as well, and thus using large supercells is critical for carrier capture calculations. This argument becomes clearer by comparing Figure with 9(b). For Sn_i in CsSnI_3, the electron capture rates outpower the hole capture rates, which are detrimental in p-type CsSnI_3 (e.g. self p-doped sample under Sn-poor condition). While avoiding Sn-poor conditions could decrease the likelihood of transitioning into SnI_4 [34] and the background hole density, a high tin chemical potential facilitates the formation of tin interstitials which lead to deep traps. This result provides an explanation of why increasing the amount of SnF_2 additives does not make the quantum efficiency of Sn-perovskites monotonically increase in experiments [35].

4. Conclusions

In summary, GGA+U+SOC provides an affordable way to calculate tin/lead inorganic perovskites incorporating both band gap correction as well as spin–orbital coupling. It also allows us to utilize large supercells for defect calculations and thus avoid potentially insufficiently relaxed structures caused by the size limitation. Within this scheme, the formation energies and transition levels of selected native defects in γ-CsPbI_3 and γ-CsSnI_3 are calculated. One-dimensional configuration coordinate diagrams are reconstructed for calculating the defect-assisted carrier capture rates for iodine interstitials in γ-CsPbI_3 and tin interstitials in γ-CsSnI_3, which are both shown to be strong minority traps under Pb-rich and Sn-poor conditions, respectively. The comprehensive theoretical research sheds light on experimentally preparing better samples for γ-CsPbI_3 and γ-CsSnI_3-based solar cells.

CRediT authorship contribution statement

Yijun Tong: Writing – review & editing, Writing – original draft, Visualization, Validation, Supervision, Software, Resources, Project administration, Methodology, Investigation, Formal analysis, Data curation, Conceptualization. **Xiaofeng Xiang:** Writing – review & editing, Validation, Investigation, Formal analysis. **Scott Dunham:** Writing – review & editing, Supervision, Methodology, Investigation, Funding acquisition, Conceptualization.

Declaration of competing interest

The authors declare that they have no known competing financial interests or personal relationships that could have appeared to influence the work reported in this paper.

Data availability

Data will be made available on request.

Acknowledgments

This work was supported in part by the NSF Materials Research Science and Engineering Center (MRSEC) program under DMR-1719797 and DMR-2308979 and by the U.S. Department of Energy's Office of Energy Efficiency and Renewable Energy (EERE) under the Solar Energy Technology Office (SETO) Award Number DE-EE0008556, This work was facilitated through the use of the Hyak supercomputer system at the University of Washington via sponsorship by the Molecular Engineering Materials Center (UW MEM-C) MRSEC, the UW Clean Energy Institute, and the UW Student Technology Fund.

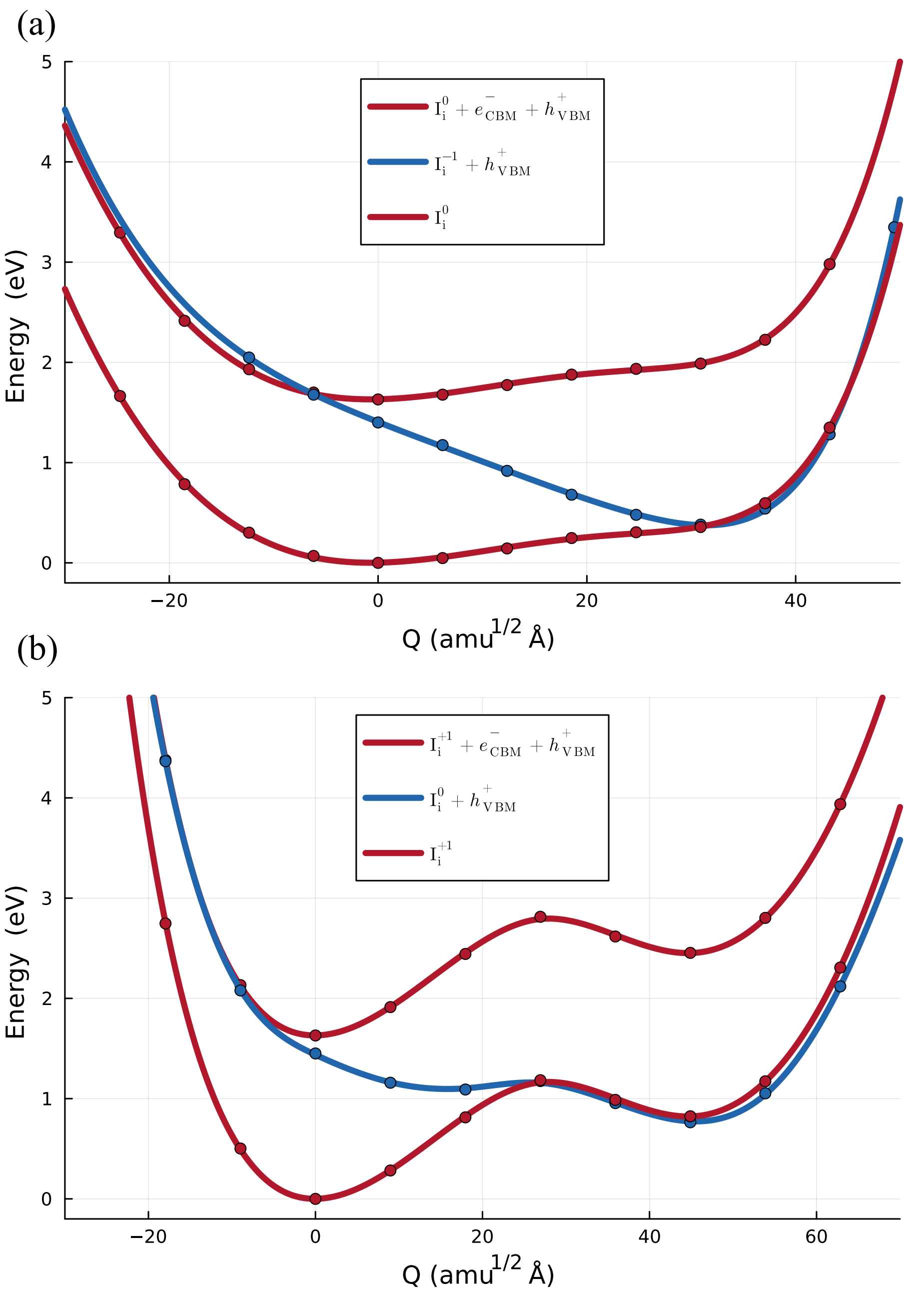

Fig. 9. Calculated one-dimensional CCDs of (a) (0/−1) and (b) (+1/0) transition levels for iodine interstitials in $CsPbI_3$(360-atom supercell).

Appendix. Thermodynamic stability of perovskites

In order to identify the available range of chemical potentials of all elements, calculation of thermodynamic stability of both perovskites are performed. For equilibrium growth of perovskites, the chemical potentials of Cs, Pb/Sn and I are related by

$$\mu_{Cs} + \mu_{Pb/Sn} + 3\mu_I = E(CsPbI_3/CsSnI_3) \tag{A.1}$$

where E is the energy from DFT calculation. To avoid formation of PbI_2/SnI_2 and CsI, the chemical potential values have to further fulfill the following constraints

$$\mu_{Pb/Sn} + 2\mu_I < E(PbI_2/SnI_2) \tag{A.2}$$

$$\mu_{Cs} + \mu_I < E(CsI) \tag{A.3}$$

and the resulting selected chemical potential values for different preparation conditions are summarized in Tables A.5 and A.6.

Table A.5
Selected chemical potential values (eV) in $CsPbI_3$.

	μ_{Cs}	μ_{Pb}	μ_I
Pb-rich	−3.0549	−1.9983	−3.064
Pb-moderate	−3.5551	−2.9983	−2.5639
Pb-poor	−4.1421	−4.1724	−1.9769

Table A.6
Selected chemical potential values (eV) in $CsSnI_3$.

	μ_{Cs}	μ_{Sn}	μ_I
Sn-rich	−3.0857	−1.8113	−3.1161
Sn-moderate	−3.4609	−2.5613	−2.741
Sn-poor	−3.7359	−3.1113	−2.4661

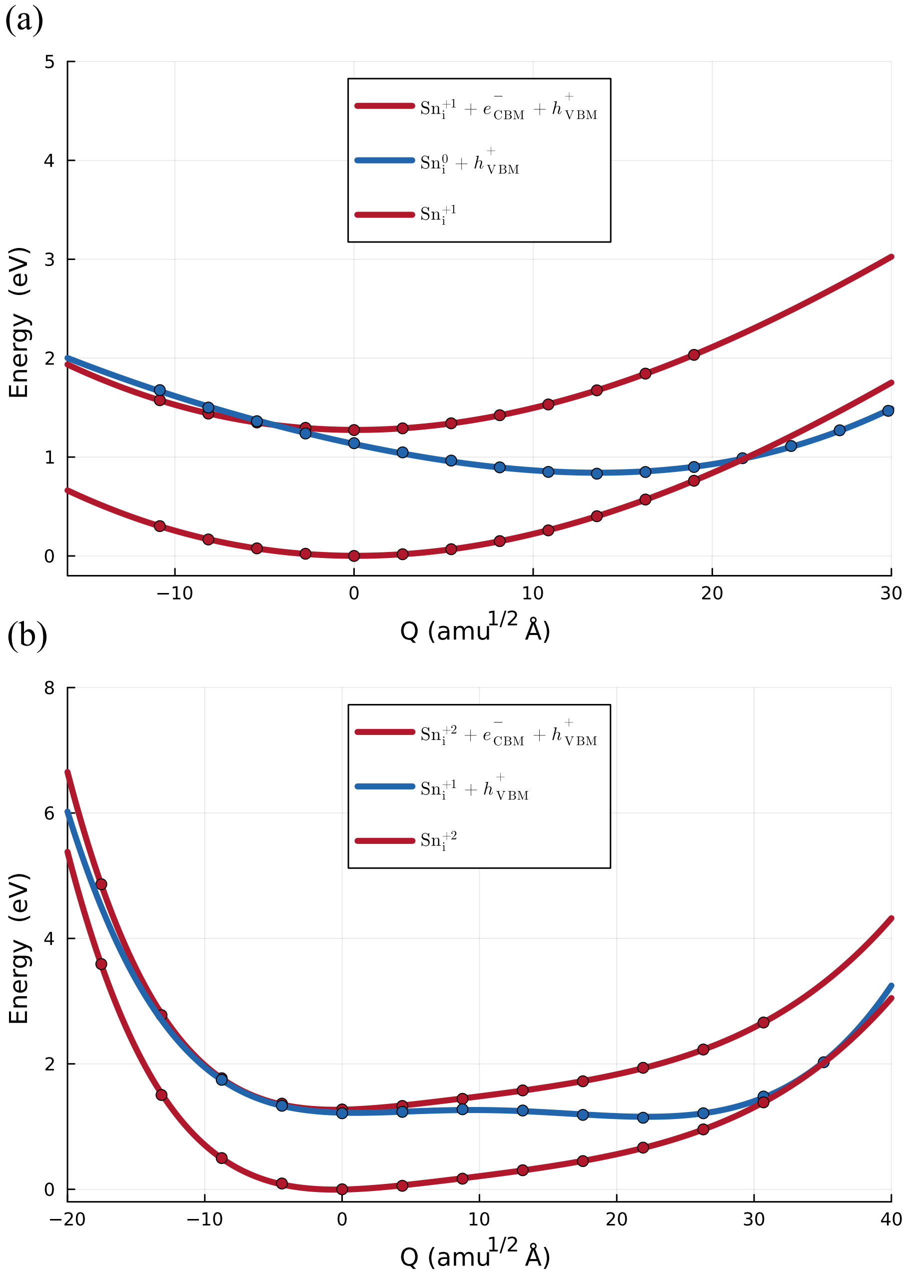

Fig. 10. Calculated one-dimensional CCDs of (a) (+1/0) and (b) (+2/+1) transition levels for tin interstitials in $\mathrm{CsSnI_3}$(360-atom supercell).

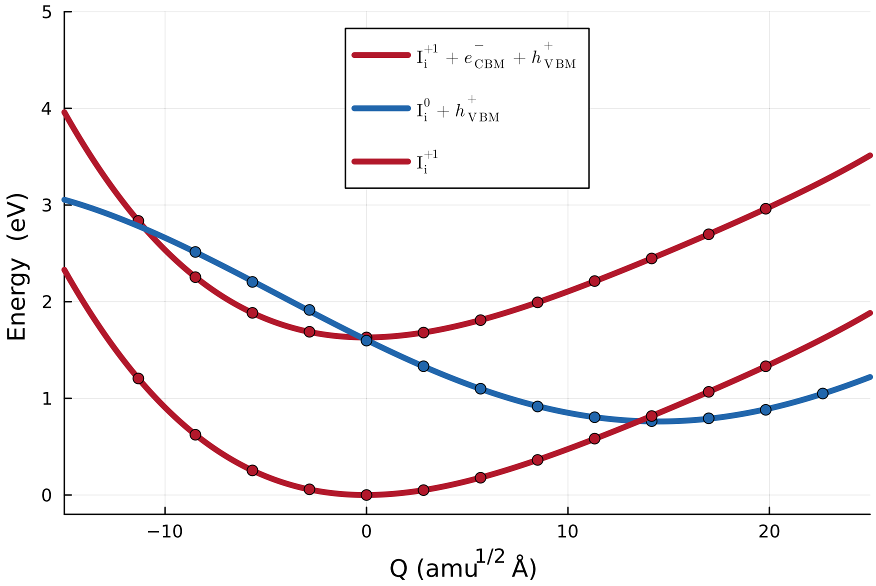

Fig. 11. Calculated one-dimensional CCDs of (+1/0) transition level for iodine interstitials in $CsPbI_3$(80-atom supercell).

References

[1] C. Vidyasagar, B.M. Muñoz Flores, V.M. Jiménez Pérez, Recent advances in synthesis and properties of hybrid halide perovskites for photovoltaics, Nano-Micro Lett. 10 (2018) 1–34.

[2] G.-H. Kim, D.S. Kim, Development of perovskite solar cells with >25% conversion efficiency, Joule 5 (5) (2021) 1033–1035.

[3] T.M. Brenner, D.A. Egger, L. Kronik, G. Hodes, D. Cahen, Hybrid organic—inorganic perovskites: low-cost semiconductors with intriguing charge-transport properties, Nat. Rev. Mater. 1 (1) (2016) 1–16.

[4] K. Lin, J. Xing, L.N. Quan, F.P.G. de Arquer, X. Gong, J. Lu, L. Xie, W. Zhao, D. Zhang, C. Yan, et al., Perovskite light-emitting diodes with external quantum efficiency exceeding 20 per cent, Nature 562 (7726) (2018) 245–248.

[5] H. Wang, Y. Sun, J. Chen, F. Wang, R. Han, C. Zhang, J. Kong, L. Li, J. Yang, A review of perovskite-based photodetectors and their applications, Nanomaterials 12 (24) (2022) 4390.

[6] I. Deretzis, E. Smecca, G. Mannino, A. La Magna, T. Miyasaka, A. Alberti, Stability and degradation in hybrid perovskites: is the glass half-empty or half-full? J. Phys. Chem. Lett. 9 (11) (2018) 3000–3007.

[7] J. Wang, J. Zhang, Y. Zhou, H. Liu, Q. Xue, X. Li, C.-C. Chueh, H.-L. Yip, Z. Zhu, A.K. Jen, Highly efficient all-inorganic perovskite solar cells with suppressed non-radiative recombination by a Lewis base, Nat. Commun. 11 (1) (2020) 177.

[8] H. Xue, G. Brocks, S. Tao, First-principles calculations of defects in metal halide perovskites: A performance comparison of density functionals, Phys. Rev. Mater. 5 (12) (2021) 125408.

[9] X. Zhang, M.E. Turiansky, J.-X. Shen, C.G. Van de Walle, Defect tolerance in halide perovskites: A first-principles perspective, J. Appl. Phys. 131 (9) (2022).

[10] C. Ming, H. Wang, D. West, S. Zhang, Y.-Y. Sun, Defect tolerance in CsPbI 3: reconstruction of the potential energy landscape and band degeneracy in spin–orbit coupling, J. Mater. Chem. A 10 (6) (2022) 3018–3024.

[11] H. Xue, J.M. Vicent-Luna, S. Tao, G. Brocks, Compound defects in halide perovskites: A first-principles study of CsPbI3, J. Phys. Chem. C 127 (2) (2023) 1189–1197.

[12] J. Zhang, Y. Zhong, Origins of p-doping and nonradiative recombination in CsSnI3, Angew. Chem. 134 (44) (2022) e202212002.

[13] X. Zhang, M.E. Turiansky, C.G. Van de Walle, Correctly assessing defect tolerance in halide perovskites, J. Phys. Chem. C 124 (11) (2020) 6022–6027.

[14] X. Wu, H. Zhang, B. Zeng, C. Ming, Y. Sun, Comparison of hybrid functionals HSE and PBE0 in calculating the defect properties of CsPbI3, J. Inorg. Mater. 38 (9) (2023).

[15] P. Giannozzi, O. Andreussi, T. Brumme, O. Bunau, M.B. Nardelli, M. Calandra, R. Car, C. Cavazzoni, D. Ceresoli, M. Cococcioni, et al., Advanced capabilities for materials modelling with Quantum ESPRESSO, J. Phys.: Condens. Matter 29 (46) (2017) 465901.

[16] J. Yang, T. Zhu, S. Liu, Onsite and intersite electronic correlations in the Hubbard model for halide perovskites, Phys. Rev. B 106 (19) (2022) 195159.

[17] M. Segall, P.J. Lindan, M.a. Probert, C.J. Pickard, P.J. Hasnip, S. Clark, M. Payne, First-principles simulation: ideas, illustrations and the CASTEP code, J. Phys.: Condens. Matter 14 (11) (2002) 2717.

[18] D.K. Paul, A.A. Hossain, A comprehensive DFT+ U investigation of electrical, optical, and structural properties of doped CsSnCl3 Perovskite: Unveiling optoelectronic potential, Comput. Mater. Sci. 231 (2024) 112585.

[19] X. Zhang, M.E. Turiansky, J.-X. Shen, C.G. Van de Walle, Iodine interstitials as a cause of nonradiative recombination in hybrid perovskites, Phys. Rev. B 101 (14) (2020) 140101.

[20] G. Kresse, J. Furthmüller, Efficiency of ab-initio total energy calculations for metals and semiconductors using a plane-wave basis set, Comput. Mater. Sci. 6 (1) (1996) 15–50.

[21] G. Kresse, D. Joubert, From ultrasoft pseudopotentials to the projector augmented-wave method, Phys. Rev. B 59 (3) (1999) 1758.

[22] J.P. Perdew, A. Ruzsinszky, G.I. Csonka, O.A. Vydrov, G.E. Scuseria, L.A. Constantin, X. Zhou, K. Burke, Restoring the density-gradient expansion for exchange in solids and surfaces, Phys. Rev. Lett. 100 (13) (2008) 136406.

[23] S. Grimme, J. Antony, S. Ehrlich, H. Krieg, A consistent and accurate ab initio parametrization of density functional dispersion correction (DFT-D) for the 94 elements H-Pu, J. Chem. Phys. 132 (15) (2010).

[24] S.L. Dudarev, G.A. Botton, S.Y. Savrasov, C. Humphreys, A.P. Sutton, Electron-energy-loss spectra and the structural stability of nickel oxide: An LSDA+ U study, Phys. Rev. B 57 (3) (1998) 1505.

[25] C. Freysoldt, B. Grabowski, T. Hickel, J. Neugebauer, G. Kresse, A. Janotti, C.G. Van de Walle, First-principles calculations for point defects in solids, Rev. Modern Phys. 86 (1) (2014) 253.

[26] C. Freysoldt, J. Neugebauer, C.G. Van de Walle, Electrostatic interactions between charged defects in supercells, Phys. Status Solidi (b) 248 (5) (2011) 1067–1076.

[27] P. Xu, S. Chen, H.-J. Xiang, X.-G. Gong, S.-H. Wei, Influence of defects and synthesis conditions on the photovoltaic performance of perovskite semiconductor CsSnI3, Chem. Mater. 26 (20) (2014) 6068–6072.

[28] S. Xiang, W. Li, Y. Wei, J. Liu, H. Liu, L. Zhu, S. Yang, H. Chen, Natrium doping pushes the efficiency of carbon-based CsPbI3 perovskite solar cells to 10.7%, Iscience 15 (2019) 156–164.

[29] H. Xie, S. Hao, J. Bao, T.J. Slade, G.J. Snyder, C. Wolverton, M.G. Kanatzidis, All-inorganic halide perovskites as potential thermoelectric materials: dynamic cation off-centering induces ultralow thermal conductivity, J. Am. Chem. Soc. 142 (20) (2020) 9553–9563.

[30] A. Liu, H. Zhu, S. Bai, Y. Reo, T. Zou, M.-G. Kim, Y.-Y. Noh, High-performance inorganic metal halide perovskite transistors, Nat. Electron. 5 (2) (2022) 78–83.

[31] A. Alkauskas, Q. Yan, C.G. Van de Walle, First-principles theory of nonradiative carrier capture via multiphonon emission, Phys. Rev. B 90 (7) (2014) 075202.

[32] S. Wang, M. Huang, Y.-N. Wu, W. Chu, J. Zhao, A. Walsh, X.-G. Gong, S.-H. Wei, S. Chen, Effective lifetime of non-equilibrium carriers in semiconductors from non-adiabatic molecular dynamics simulations, Nat. Comput. Sci. 2 (8) (2022) 486–493.

[33] Y. Kumagai, Finite-size corrections to defect energetics along one-dimensional configuration coordinate, Phys. Rev. B 107 (22) (2023) L220101.

[34] L. Lanzetta, T. Webb, N. Zibouche, X. Liang, D. Ding, G. Min, R.J. Westbrook, B. Gaggio, T.J. Macdonald, M.S. Islam, et al., Degradation mechanism of hybrid tin-based perovskite solar cells and the critical role of tin (IV) iodide, Nat. Commun. 12 (1) (2021) 2853.

[35] A. Treglia, F. Ambrosio, S. Martani, G. Folpini, A.J. Barker, M.D. Albaqami, F. De Angelis, I. Poli, A. Petrozza, Effect of electronic doping and traps on carrier dynamics in tin halide perovskites, Mater. Horiz. 9 (6) (2022) 1763–1773.